Maritime Field Trial of a Dual-Band Silicon Integrated Photonics-Based Radar

Giovanni Serafino, Salvatore Maresca, Claudio Porzi [ID], Filippo Scotti [ID], Antonio Malacarne [ID], Malik Muhammad Haris Amir [ID], Paolo Ghelfi [ID], and Antonella Bogoni

(Invited Paper)

Abstract—This paper reports the development, the complete characterization, and the first outdoor field trial of a coherent dual-band photonics-based radar implemented through integrated photonic circuits. The dual band radar transceiver has been implemented on a silicon-on-insulator platform, and is capable of operating up to the Ku-band. It has been packaged and engineered on a printed circuit board for its use in a complete radar system. The electronic RF front-end in S- and X-bands and the digital baseband equipment have been developed in order to guarantee performance aligned with the state of the art of conventional radars. The developed apparatus has been characterized in S- and X-band in terms of sensitivity, linearity, phase noise, and conversion efficiency, both at chip and system level. The impact and issues related to the used fabrication platform and to the packaged approach have been analyzed. The outdoor field trial has been carried out in a relevant maritime environment close to the port of Livorno (Italy). First, X-band radar acquisitions of a complex maritime scene using a rotating antenna has allowed to verify the radar behavior by comparing the detected scene with official data provided by the automatic identification system mounted on the observed ships. A false alarm probability of 2×10^{-5} has been demonstrated, aligned with radar state of the art. Then, S- and X-band range/velocity acquisitions allowed to confirm the coherent dual band operation, posing the basis for the next step: the development of adapted coherent data fusion algorithms for target imaging.

Index Terms—Photonic integration, silicon photonics, radar system, dual band operation.

I. INTRODUCTION

RADAR systems are part of our everyday life. Originally invented at the beginning of the 20th century as a powerful tool in the navy battlefields, it is now used for controlling the maritime traffic, guiding airplanes during takeoff and landing, studying the Earth atmosphere from ground and from satellite, listening the breath of volcanos, avoiding car collisions in traffic, pushing the automation in the industry, measuring the vital signs in patients.

The basic working principle of a radar is to transmit a radio frequency (RF) signal and to measure its back scattered echo in order to estimate the distance and velocity of a reflecting target [1], [2]. But depending on the application, different waveforms and frequencies can be used, for example for trading-off the observable distance, the resolution, the robustness to weather conditions, and so on.

In the last few decades, the concept of multiband radar has been introduced to simplify the management of multiple radar systems, increase the amount of information detected by a single system, and overcome the bandwidth limitations posed by spectrum usage regulations [3]–[5]. In fact, multiband radars can gain performance by taking advantage of the peculiarities of each different frequency band, e.g., the low atmospheric attenuation of the lower frequencies [6], or the high fractional bandwidth available at higher carrier frequencies, with increased sensitivity to Doppler shift given by a moving target [7]. Moreover, since the resolution R of a radar system is given by the signal bandwidth B through the well-known relation $R = c/2B$ with c the speed of light, fusing together the information from multiple bands also means increasing the nominal radar resolution.

However, multi-band radars still are not common, due to the complexity of the required circuitry that needs to manage different RF frequencies simultaneously, typically involving different oscillators, mixers and filters, with consequent very large encumbrance and significant electromagnetic interferences.

A possible simplification in the development of multiband radars could come from the use of microwave photonics techniques, i.e., using photonics for implementing microwave systems [8], [9]. In particular, in the last years photonics has gained lot of attention for the implementation of radar systems, not only ensuring specific advanced functions such as extremely low phase noise, ultra-wide bandwidth, and large frequency flexibility [10]–[13], but also providing a complete radar transceiver [14], even with the capability of flexible and multiband operation [15]–[19]. More recently, the rapid development of photonic integration technologies has also led to the on-chip
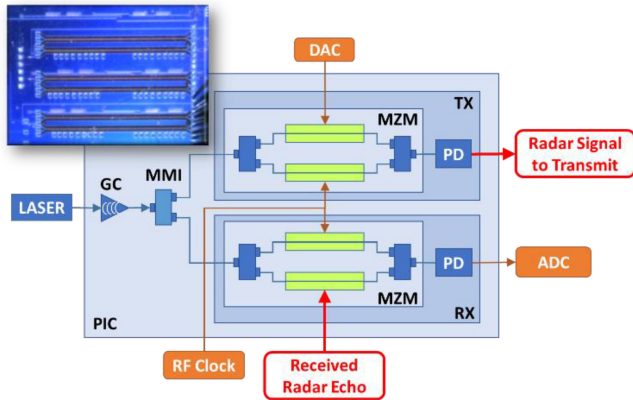
Fig. 1. Architecture of the photonics-based multiband radar transceiver, with indication of input and output ports (optical, IF, or RF). The green boxes identify the active p-n junctions in the modulators arms. The inset shows a picture of the PIC.

implementation of photonics-based radars, targeting applications demanding very reduced size, weight, and power consumption (SWaP) [20]–[22].

In [23] and [24], we have presented the preliminary results of a photonic integrated circuit (PIC) based on silicon-on-insulator (SOI) platform implementing a photonics-based multiband radar transceiver. The PIC is capable to operate from the S-band up to the Ku-band simultaneously, requiring only a single low frequency RF reference clock [23], and it has been packaged to be able to operate up to the X-band and engineered on a printed circuit board (PCB) for easy control, in order to allow its use in an indoor field trial [24].

In this paper, we present the overall design and implementation of this PIC, the development of a complete dual-band radar system exploiting the packaged PIC, and the first outdoor field trial in a real maritime scenario. The results allow to demonstrate the fully functionality of such multiband radar system, operating in both S- and X-band, with operative detection capability suitable to real maritime traffic.

The paper is organized as follows: Section II presents the design, fabrication, and characterization of the PIC; Section III describes the PIC packaging approach, implementation, and characterization, which allows the use of the photonics-based solution in complex setups; Section IV describes the realization of the maritime outdoor field trial, including the implementation of the S- and X-band front-ends and their characterization, and the detection results from the real scenario; Finally, Section V discusses the obtained results and outlines the conclusions.

II. PHOTONIC INTEGRATED RADAR TRANSCEIVER

The general architecture of the integrated photonics radar developed in [23], [24] is shown in Fig. 1.

The system has been designed in SOI platform. This technical choice has been driven by the technological maturity of the SOI platform in integrating passive components, electro-optical modulators, and photodiodes [25].

With reference to the architecture of Fig. 1, since monolithic SOI does not have lasing capabilities, a laser source is considered

to be coupled into the PIC through a vertical grating coupler (GC) that allows the signal to be distributed to its internal circuit. Once inside the PIC, the laser signal is split by a 1×2 multimode interference (MMI) splitter to feed both the transmitter (TX) and the receiver (RX) sections of the radar. Both sections are composed of a Mach-Zehnder modulator (MZM) followed by a Si-Ge photodiode (PD).

In both the TX and RX sections, one arm of the MZM is driven by a reference RF clock signal at frequency f_{CK} to generate an optical comb inside the MZMs. To achieve this, the RF clock signal is strongly amplified and split to drive one arm of both TX and RX MZMs. Several optical modulation sidebands are generated inside the MZMs, due to the high modulation voltage of the RF clock signal, at $\pm f_{CK}$, $\pm 2f_{CK}$, $\pm 3f_{CK}$, $\pm 4f_{CK}$, etc. from the laser.

In the transmitter MZM, the second arm is driven by a signal generated by a digital-to-analog converter (DAC) centered at intermediate frequency (IF) f_{IF}. At the transmitter photodiode, the optical tones generated by the RF comb beat with the optical sidebands generated by the DAC, performing the RF up-conversion of the IF signal to several multiples of the clock frequency, following the equation $f_{RFn} = n \cdot f_{CK} \pm f_{IF}$. After being up-converted, each signal f_{RFn} is sent to a specific frontend that is in charge of filtering and amplifying the specific up-converted radar signal. Multiple signals at IF can be applied at the same time, so that multiple RF signals can be generated simultaneously.

Similarly, the received radar echo at f_{RF}, or multiple echoes at different RF frequencies, drives the second arm of the RX MZM, and the RX PD performs the down-conversion to the original f_{IF}, which can be acquired by an analog-to-digital converter (ADC) and processed by a digital signal processing unit.

After being designed, the architecture represented in Fig. 1 has been sent to fabrication in a multi-wafer project run at the foundry IMEC. A picture of the PIC is reported in the inset of Fig. 1.

The characterization experiments [23] have been performed using an external continuous-wave (CW) laser source at 1550 nm, with 15 dBm output power. The laser linewidth is less than 100 kHz, although this parameter does not affect the performance of the integrated radar architecture (due to the physical dimensions of the PIC in the order of few mm). The laser is coupled to the PIC through the input GC. Bias-tees are used to apply the electrical signals driving the MZM to the PIC, in order to consent proper biasing of the p-n junctions implementing the phase shifters in the two arms of the MZMs (green boxes in the MZM in Fig. 1). First of all, the bandwidth of the MZM and of the PD that act as electro-optical and opto-electrical conversion blocks respectively, have been verified. The measured bandwidth of the modulator is 20 GHz, while the measured bandwidth of the photodiode is >20 GHz.

A synthesizer generates the reference RF clock at $f_{CK} = 3.5$ GHz. Fig. 2(top) reports the RF spectra produced after the radar Tx PD output when the corresponding DAC is set to generate a plain radar pulse with a duration of 2 μs and a pulse repetition interval (PRI) of 40 μs, centered at $f_{IF} = 100$ MHz. As can be seen, clear replicas of the IF signal are generated at S band
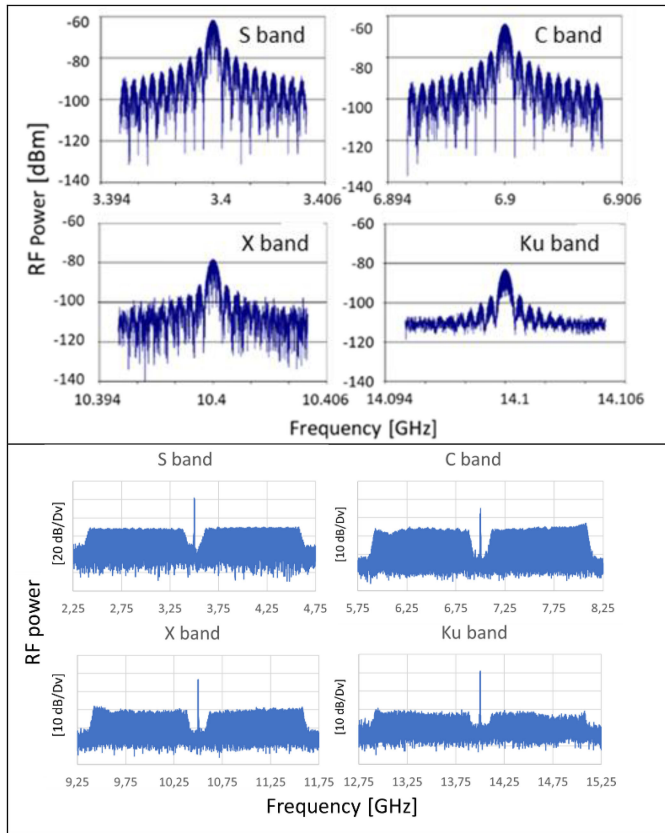
Fig. 2. Radar signal generated in the S, C, X and Ku band in case of (a) 2 μs pulses with a pulse repetition interval (PRI) of 40 μs, centered at $f_{IF} = 100$ MHz and (b) 2 μs pulsed waveform with a superimposed chirp with a bandwidth of 1GHz at $f_{IF} = 100$ MHz.
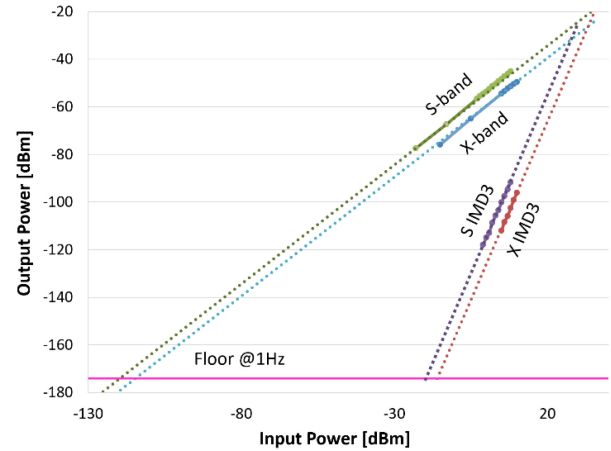

Fig. 3. Two-tone analysis for the radar PIC in S- and X-band. The graph reports the first harmonic and the intermodulation distortion of the third order (IMD3), as well as the noise floor.

(3.4 GHz, Fig. 2(a)), C band (6.9 GHz, Fig. 2(b)), X band (10.4 GHz, Fig. 2(c)), and Ku band (14.1 GHz, Fig. 2(d)), confirming the capability of the radar PIC to perform up-conversion of the signal to several output frequencies generated as a multiplication of the clock signal. The receiver radar section implements the down-conversion function with similar performance. In order to verify the wideband benefit introduced by the use of photonics, Fig. 2 (bottom) shows the generation by the PIC of a wideband signal represented by 2 μs pulsed waveform with a superimposed chirp with a bandwidth of 1 GHz.

Fig. 3 shows the spurious-free dynamic range (SFDR) two-tones analysis of the radar receiver section. The analysis has been run for the S and X bands only, given the available RF equipment in the lab for amplifying and filtering the driving RF signal tones. The graph shows the values of the first harmonic and of the third-order intermodulation distortion. The level of the thermal noise of the PD is also reported at −174 dB.

The RF-to-IF conversion loss in X band turns out to be 59 dB, with a SFDR of 99 dB·Hz$^{2/3}$. For the S band in the other hand, the conversion loss is 55 dB, and the SFDR results to be 100 dB·Hz$^{2/3}$. While the value for the SFDR is enough for managing the requests on dynamic range of several radar applications [1], [2], the conversion loss is dramatically high. For comparison purposes, we take as reference the conversion loss values reported in [21] for a similar microwave-photonics RF transceiver

implemented in SOI. For that work, the declared conversion loss goes from 40 to 60 dB for signals in the frequency range from 2 to 10 GHz, which is in line with the values reported here, and are thus typical of a microwave photonic transceiver in SOI. Even though the values are worse than the conversion losses of standard RF systems (for RF mixers the conversion loss can be <20 dB), these systems have a remarkable frequency flexibility, which is confirmed by the similar results obtained for the two largely detuned analyzed bands. The rather high values of conversion loss can be ascribed to a number of factors, the most apparent being the PIC insertion loss, the optical power of the laser, and the half-wave voltage of the modulator (Vpi).

For what concerns the optical loss, it must be considered that the PIC has a monitor splitter between the MZM and the PD at the TX section (not reported in Fig. 1), and removing it would allow recovering 3 dB in the optical domain, improving the conversion loss by 6 dB. Moreover, a more powerful laser (or a laser followed by an optical amplifier) could be used as optical source, increasing the launching power up to the limit posed by the two-photon absorption in the SOI waveguide. Finally, the modulators used here are standard library components with a Vpi = 10 V, which could be reduced by increasing the MZM length, finding a specific trade-off between the Vpi and the optical loss of the modulators for MWP applications.

As described in [23], in order to test the radar functionality of the bare PIC, the monitoring testing point after the TX MZM has been used to feed a fiber-based radar target emulator. After being routed out of the PIC through the monitoring GC, the optical signal is delayed in an optical fiber spool of 1 km length and sent to an external photodiode (chosen with similar performance to the integrated PD). The radar signal at the desired frequency is then filtered in the electrical domain and amplified by a chain of low-noise amplifiers (LNAs). A variable attenuator is inserted after the LNA to consent varying the RF power at the radar receiver input. This scheme is used to perform the characterization tests of the PIC as a radar system.

As reported in Fig. 4, we evaluate the radar performance of the PIC by measuring the system sensitivity.
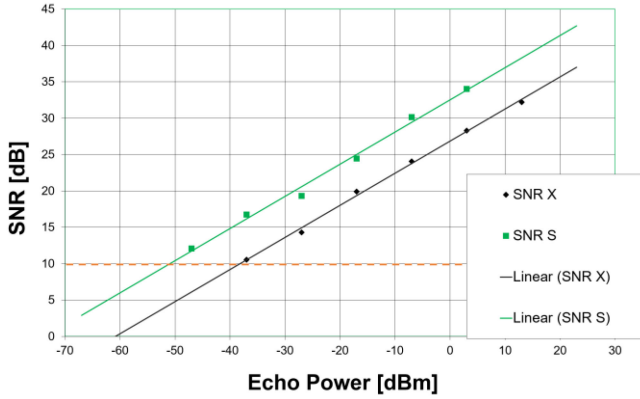
Fig. 4. Radar PIC sensitivity in S- and X-band, calculated as the minimum detected signal ensuring a SNR > 10 dB.

Fig. 5. Packaged chip on the control board.

TABLE I
PERFORMANCE COMPARISON BETWEEN BARE AND PACKAGED PIC

	Bare PIC		Packaged PIC	
	S-band	X-band	S-band	X-band
Conversion Loss [dB]	55	59	59	65
SFDR [dB·Hz$^{2/3}$]	100	99	95	93

Since every radar processing is based on the cross-correlation of the received signal with the transmitted waveform, here the sensitivity is defined as the signal-to-noise ratio (SNR) of the cross-correlation signal, calculated after the down-conversion and digitization in an ADC. A 2 μs-long linearly chirped pulses with a bandwidth (BW) of 100 MHz is used, integrating the echoes for 20 ms. As calculated from the results in Fig. 4, the minimum detectable echo power is -52 dBm and -38 dBm for the S and X bands respectively, considering a minimum acceptable SNR of 10 dB as reference value [2]. Please note that the SNR value impacts on the performance of the complete radar system in term of probability of detection and of false alarm, while the minimum detectable signal affects the maximum detectable range and/or the minimum radar cross-section (RCS) of a detectable target. These results do not consider any electrical front-end, as they are measured directly at the radar chip input. In case of amplification stages, the radar sensitivity would be substantially improved, as will be demonstrated below.

In summary, the developed radar PIC shows an ultra-wideband frequency-flexibility with simultaneous multiband capability in a single ultra-compact integrated device. The tests report linearity and sensitivity in line with the main radar applications.

III. PACKAGED RADAR PIC

The PIC described above has been inserted in a functional package for allowing an agile utilization in a whole radar system setup, targeting its usage up to the X band (Fig. 5). The functional package considers placing the PIC on a PCB acting as a fan-out for the RF and DC pads, providing an easy access to electrical signals and controls. For reducing as much as possible the loss and parasitic inductance of the wire bonds, a rectangular hole has been dug in the center of the PCB to host the PIC, so that the top surface of the PIC and of the PCB are at the same level, and the length of the wire bonds is minimized (inset in Fig. 5). The PIC is also laid on a thermo-electric cooler (TEC) for thermal stabilization, and a thermistor is glued on the top of the PIC for reading the instantaneous temperature. The PIC is pigtailed with a fiber array to get access to the GC for the input laser. Finally,
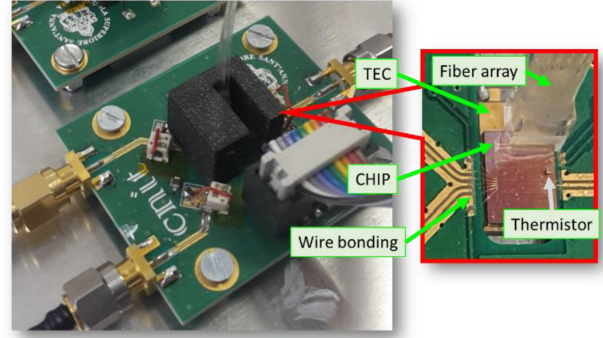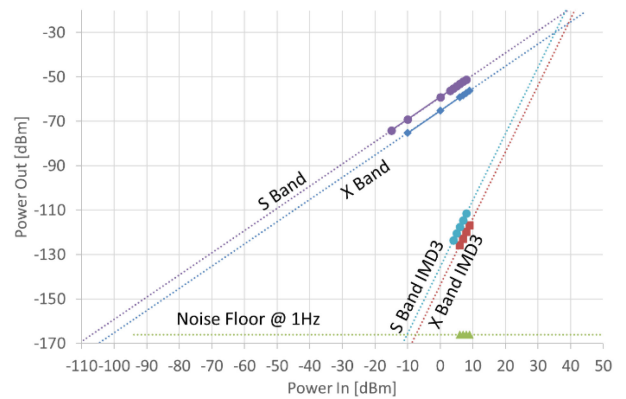

Fig. 6. Two-tone analysis of the packaged PIC in S- and X-band.

a custom 3D-printed plastic cover is placed above the PIC for protection.

In order to simplify the design of the PCB, instead of implementing a single PCB with several RF traces, we have opted for developing one packaged PIC for the TX and one for the RX. By taking advantage of the symmetric structure of the TX and RX sub-blocks in the PIC architecture (Fig. 1), the two PCBs are identical, implementing a modular approach.

The design of the PCB has been obtained through a finite-element electromagnetic simulation program. The PCB includes standard connectors for DC controls and RF input/output signals, as well as bias-tees for correctly biasing the p-n junctions of the modulators and the PD on the PICs.

The TX and RX packaged PICs have been characterized in S- and X-band with a two-tone test, in order to verify the penalty induced by the packaging compared with the bare chip, in terms of conversion loss and SFDR. The results of the test are summarized in Table I, while Fig. 6 reports the case of down-conversion from S- and X-band to IF. In the worst case
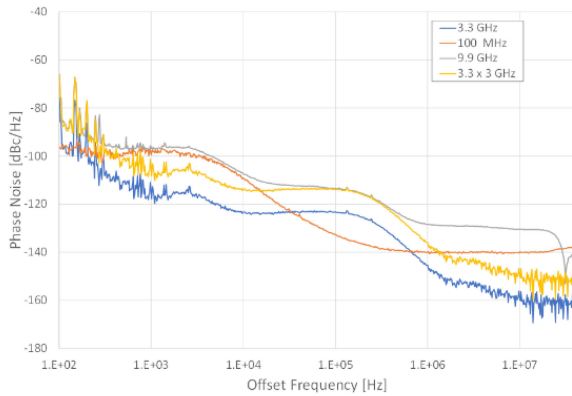
Fig. 7. Phase noise of the signal generated at 9.9 GHz, and of the signals that determine it.

TABLE II
REQUIREMENTS FOR THE OPERATIVE SCENARIO

Max Distance	Min RCS	Max PFA	Min sensitivity
≥ 2 km	≥ 100 m^2	$\leq 10^{-5}$	≤ -78 dBm

(X-band), the penalty introduced by the packaging is about 6 dB for both the SFDR and the conversion loss, making this last value even more critical. In this case the noise floor value is -166 dB.

As reported in [24], we have also investigated the phase noise of the RF signals generated by using the packaged PIC. In this analysis, we have used an RF clock at 3.333 GHz generated by a synthesizer, and a sinusoidal radar waveform at $f_{IF} = 100$ MHz generated by the DAC. After the PD, we analyze the phase stability of the up-converted radar signal at 9.9 GHz. An appropriate RF filter has been used to select the output signal from the PIC and supply it to the measuring instrument (Signal Source Analyzer).

The result of the analysis is reported in Fig. 7. The figure reports the phase noise of the signal generated at 9.9 GHz, compared with the phase noise of the RF clock at 3.333 GHz, and of the IF signal at 100 MHz. A curve showing the theoretical phase noise of the third harmonic of the RF clock at 10 GHz is also reported, which corresponds to a translation of the phase noise of the RF clock upwards of $20 * \log(3) = 9.5$ dB, where the log argument 3 is the frequency multiplication factor. In principle, the phase noise of the output signal at 9.9 GHz should coincide with the phase noise of the multiplied clock at 10 GHz (neglecting the effect of the small frequency difference). Then, the signal should also be affected by the noise of the IF signal. Actually, the grey curve in Fig. 7 relative to the signal at 9.9 GHz follows well the yellow curve related to the multiplied clock at 10 GHz for the central range of offset frequencies, while it follows the curve of the IF signal (orange curve) at lower frequencies. Finally, the low power emitted by the PIC causes the measurement instrument to reach its noise floor for the higher frequencies.

IV. OUTDOOR FIELD TRIAL

Using the packaged PICs described above, a complete dual band radar system (i.e., including RF front-ends and radiating antennas) has been developed, characterized and tested in an outdoor field trial considering a relevant maritime scenario: the surveillance of the traffic in the area surrounding the port of Livorno (Italy). Discussions with authorities and final users has

led to the definition of the minimum requirements for this field trial scenario, as reported in Table II. A minimum distance of 2 km should be observed, and the radar should be able to see all the echoes above a sensitivity of -78 dBm. The detection of all targets with a minimum RCS of 100 m^2 (corresponding to a fishing boat of medium dimensions) should be guaranteed with a probability of false alarm (PFA) $< 10^{-5}$.

The experimental setup used for the field trial is reported in Fig. 8. The two packaged PICs (one for TX, one for RX) are fed by two CW lasers at 1550 nm with an output power of 15 dBm each. Two polarization controllers (Polctrls) set the polarization state of the lasers to correctly couple into the PICs.

The RF clock is provided by a synthesizer. In this case, the clock frequency has been set at 2.5 GHz. The clock is then amplified at 30 dBm by a high-power amplifier (HPA) and split into two arms, each feeding the input RF clock port of one PCB at 27 dBm.

The digital part of the setup includes a 400 MSa/s DAC providing an output power of 20 dBm (enough to correctly drive both the PICs), and a 400 MSa/s ADC. The signal at IF provided to the ADC by the RX PIC is amplified by two amplifiers (20 dB of gain each) to match the dynamic range of the ADC itself, and low-pass filtered at 200 MHz to prevent aliasing and to reduce the noise contributions. In this field trial, the DAC is programmed to generate two signals at two different IF, in more detail: IF$_S = 75$ MHz and IF$_X = 125$ MHz. Both waveforms are 2 μs-long radar pulses with a linear frequency chirp of 20 MHz and a PRI of 100 μs. These radar signals are then up-converted by the TX PIC to the S- and X-bands at 2.575 GHz and 9.875 GHz, respectively.

The transmitter side of both the front-ends in S- and X-band are realized cascading cavity band-pass filters with a bandwidth of 20 MHz, multiple LNAs providing about 50 dB of gain, and one HPA for each front end (with a maximum output power of 100 W in the case of X-band, and 20 W for the S-band, high enough for covering the maximum distance requested by the operative scenario). The X-band front-end also shows two switches: they are driven in off mode when the radar is not transmitting the pulse, to suppress the strong noise from the HPA that could blind the receiver section. The S-band front-end instead could count on one switch only. For this reason, while the X-band radar is implemented in monostatic configuration (i.e., with one antenna only, including a circulator to separate the TX and RX operations), the S-band is implemented in bistatic configuration (i.e., with two separate antennas for TX and RX).

The radar echoes captured by the receiver antennas pass through the receiving section of the front-ends, including cavity band-pass filters, LNAs and switches, similarly to the front-ends transmitting sections. A variable attenuator for each band is also inserted for adapting the signals level to the correct values
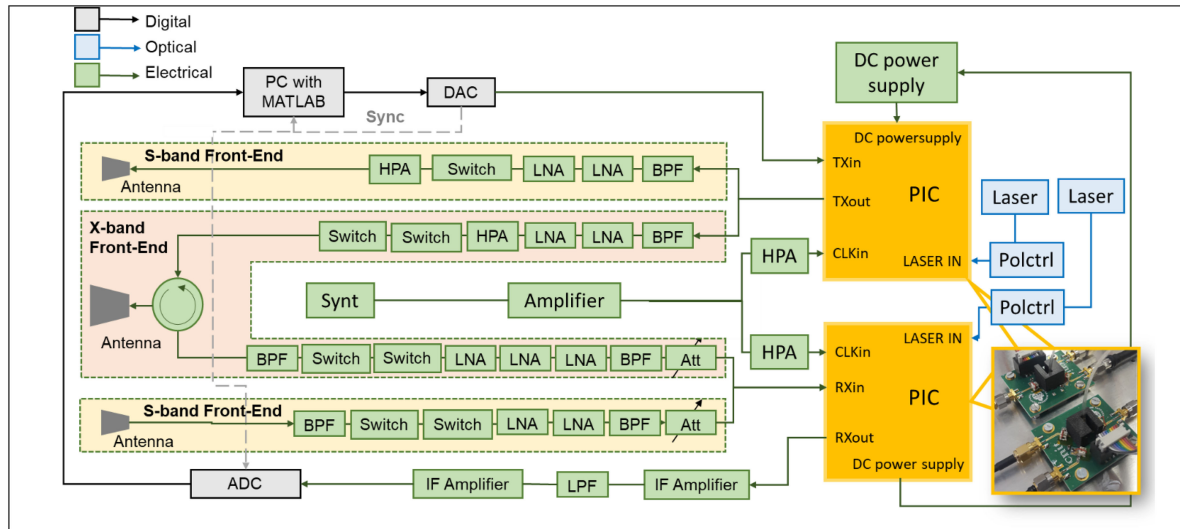
Fig. 8.   Experimental setup of the outdoor field trial for the dual-band photonics-based radar demonstration.
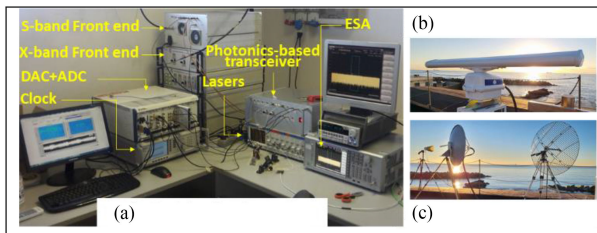

Fig. 9.   (a) Picture of the experimental setup used for the radar outdoor field trial. (b) X-band rotating antenna used for the single band acquisition. (c) Antennas for dual-band acquisitions: X-band parabolic antenna in monostatic configuration (center), and S-band parabolic (right) and horn (left) antennas in bistatic configuration.

Fig. 10.   Two-tone analysis of the complete radar system in S- and X-band.

for driving the PIC. Finally, the received signals from both the S- and X-bands are simultaneously routed to the receiver PIC.

A specific system control tool has been developed to run the field trial. It includes a PC with an FPGA managing the acquisition of the sample flow from the ADC, and a MatLab tool that operates a standard radar processing: each IF signal (at 75 MHz for the S-band, and at 125 MHz for the X-band) is first digitally down-converted to baseband, thus obtaining complex samples; then, a number of samples corresponding to the coherent integration time (CIT) are organized in a matrix of M rows and N columns, where N represents the number of samples in a single PRI, and M the number of pulses to be coherently integrated. The cross-correlation between the single received pulse and the reference baseband signal (obtained directly from the transmitted waveform parameters) is performed on each line. Subsequently, a Fast Fourier Transform is made on each column, and the square modulus of each complex sample is calculated. This matrix represents the range/Doppler map of the observed scenario.

A picture of the complete setup is reported in Fig. 9(a), where the engineered photonics-based radar transceiver that includes the packaged PICs for TX and RX, the thermo-electric cooler (TEC) controllers, and the power suppliers, can be recognized.
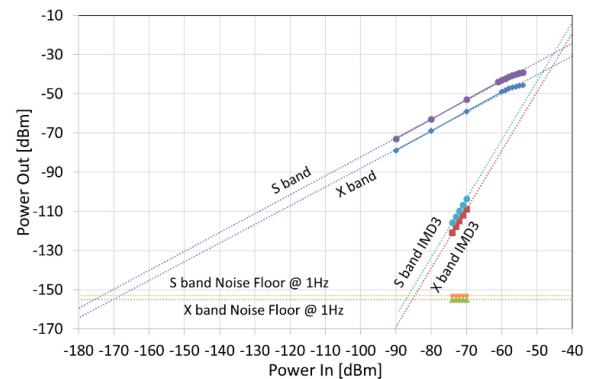
The front-ends for the X-band and S-band are also visible, as well as the digital part of the system (DAC and ADC), the RF clock generation, the feeding lasers, and the electrical spectrum analyzer (ESA) used for diagnostic purposes.

The dual-band radar system (i.e., the packaged PICs plus the front-ends in S- and X-band) is first characterized with a two-tone analysis, as reported in Fig. 10. For the X-band, a SFDR of $81 \text{ dB} * \text{Hz}^{2/3}$ and a conversion gain of 11 dB is measured, while the S-band reports a SFDR of $83 \text{ dB} * \text{Hz}^{2/3}$ and a conversion gain of 17 dB. As can be seen, the use of the front-ends on the receiver side allows to totally recover the conversion loss of the radar system and to finally obtain a conversion gain (see Table I for comparison), but this comes at the expense of an increased noise floor. It is -153 dB and -155 dB for S and X band respectively. The two different values are due to the use of two different front ends. It is also interesting to note that the S-band front-end is noisier than the X-band, so its noise floor is higher. Moreover, the amplification chains of the front-ends also induces an increase of the 3$^{\text{rd}}$-order intermodulation distortion (IMD3). As a result, the measured SFDR is significantly reduced for both the frequency bands, but still enough for the field trial application.
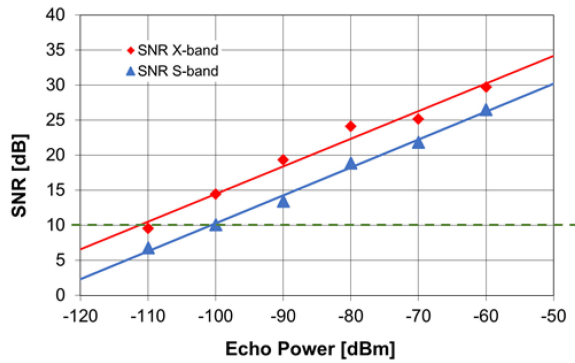
Fig. 11. Sensitivity of the complete radar system in S- and X-band.

Fig. 12. Single-band observed maritime scene, with indication of the present targets. The insets report the zooms and names of the targets. The targets with & without AIS are indicated in yellow and red, respectively.

Fig. 13. Spatial map of the radar acquisition with the official position of the vessels equipped with the AIS.

The analysis of the sensitivity of the complete dual-band radar system, obtained testing the system in back-to-back configuration with the use of a variable attenuator at the receiver input, is reported in Fig. 11 in the same condition of Fig. 4 (i.e., with 2 μs-long linearly chirped pulses with a bandwidth of 100 MHz and integrating the echoes for 20 ms). The graph reveals a minimum detectable signal of -110 dBm in X-band and -100 dBm in S-band, still well above the requirements defined by the operative scenario (< -78 dBm).

Finally, the field trial has been performed. First, a single-band experiment has been conducted for confirming the effectiveness of the proposed system through a comparison with official data provided by the Automatic Identification System (AIS) of the vessels that are navigating in the area under observation. This area is depicted in Fig. 12, together with the zooms and names of all the visible targets (see insets in Fig. 12), and the indication about the availability of AIS data. We can note that the observed scene includes four big vessels with AIS, and few small boats without AIS. Moreover, the lighthouse of the port is also clearly visible.

The scene under observation has been acquired in X-band using a rotating antenna (see Fig. 9(b)) consisting in a 6-feet slotted waveguide array with a central frequency of 9.875 GHz, a horizontal and vertical beam width of about 1° and 25° respectively,
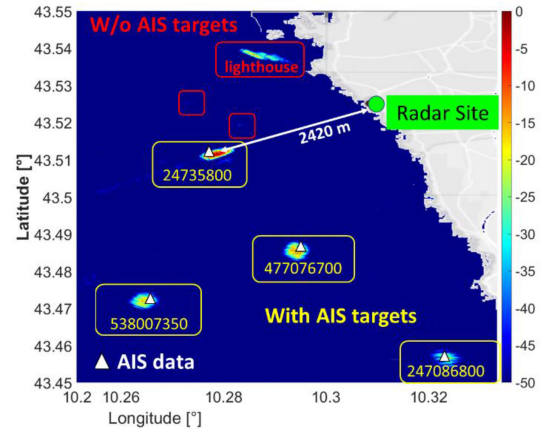
a gain of 30 dB, and a rotation speed of about 27 revolutions per minute. Naming as range direction the direction from the radar to the target, and cross-range direction the orthogonal direction on the same plane, the 1° horizontal beam width of the antenna determines the cross-range resolution (for example, it is equal to about 20 m at a distance of 1 km from the radar), while the range resolution is given by the 20 MHz bandwidth of the radar signal, corresponding to 7.5 m. The CIT has been set to 7.5 ms, which corresponds to a rotation of 1° for the antenna. Given the PRI of 100 μs, the unambiguous range is 15 km, much larger than the requested maximum distance defined in Table II.

Fig. 13 reports the acquisition map obtained with the X-band radar and the rotating antenna. The radar site is highlighted in green. The official positions of the four vessels equipped with AIS are also reported (white triangles). It is evident that the photonics-based radar is able to reveal the correct position of all the vessels. It should be noted that the AIS data and the radar acquisitions are not synchronous, therefore the position comparison can be affected by the slow movement of vessels. It is important to highlight that the good sensitivity of the proposed radar also allows to see small sailing boats (w/o AIS) and the port lighthouse, which both have a RCS largely smaller than the minimum requested value (see Table II).

The same configuration has been used to calculate the false alarm rate of the radar system.

In the same scenario, we exploited 25 rotation loops of the antenna for evaluation of the probability of false alarm.

This measure has been obtained collecting the acquisition data from 25 rotation loops of the antenna, and running a detection algorithm able to distinguish detection cells with true targets (which are detected in the same cell for a number of rotation loops above a fixed threshold) from the cells with false alarms (which are present in a cell for a number of loops below the fixed threshold). The number of detection cells is given by the number of range resolution cells for each pointing angle (i.e., the unambiguous range divided by the range resolution, in our case 15000:7.5 = 2000), multiplied by the number of Doppler cells (i.e., the CIT divided by the PRI, in our case 10E-3:100E-5 = 100), multiplied by the number of pointing
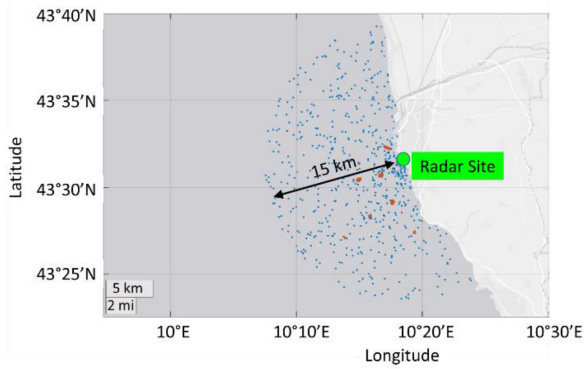
Fig. 14. True targets and false alarms detected in 25 antenna rotation loops.
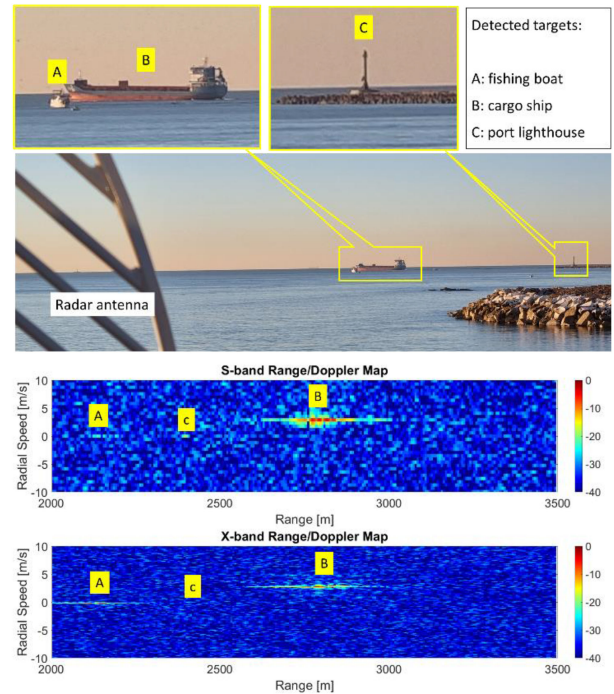

Fig. 15. Top: maritime scene observed with the dual-band acquisition with indication of the present targets. In the insets, the targets zooms and categories are reported. The radar antenna site is also visible. Bottom: range/Doppler maps obtained with coherent acquisitions in S- and X-band with indication of the targets.

direction (in our case about 180 sectors of 1° each), multiplied by the number of antenna loops (in our case 25). The final number of total acquisition cells is 900 million. Fig. 14 reports the true targets (red) and all the false alarms (blue) for all the acquisition cells (including those with Doppler different from zero) superimposed in a single plot. Counting the false alarms, this corresponds to a false alarm probability of $2 * 10^{-5}$: a reasonable number for a maritime case, and very close to the minimum requirement of the considered operative scenario.

Once the effectiveness of the X-band radar has been confirmed, a dual-band detection has been performed for verifying the coherent multiband operation. In this case, the rotating antenna in X-band has been replaced with a parabolic antenna with a gain of 30 dBi and a field of view of 10° (see Fig. 9(c)). With reference to the same Fig. 9(c), a similar parabolic antenna with the same performance has been used at the transmitter side for the S-band, while at the receiver side a horn antenna with 10 dBi of gain and 20° aperture has been used, in a bistatic configuration. All the three antennas have been pointed manually towards specific targets. Fig. 15 (top) reports the case of one observed scene, while in the insets a zoom of the present targets is shown, including a small fishing boat (A), a cargo ship (B), and the port lighthouse (C).

In Fig. 15 (bottom), the range/Doppler maps obtained with coherent acquisitions in S- and X-band are reported. The small fishing boat at a range of 2140 m, the lighthouse at 2400 m, and the big cargo ship at 2800 m are visible with the same resolution for both bands. The lighthouse is less evident in X-band, probably due to a worse manual pointing, being the lighthouse placed at the edge of the antenna angle of view. In this case, the CIT has been extended to 100 ms to increase the Doppler resolution. As can be seen, the detected speed has a better resolution in X-band (i.e., 0.15 m/s) due to the higher carrier frequency, as results from the theory [1], [2]. A null speed for the lighthouse and for the fishing boat (which was not moving) has been correctly revealed. The detected speed of the cargo ship is 2.9 m/s (i.e., 10.4 km/h), which is in accordance with the data acquired by the AIS.

The S- and X-band radar signals have been verified to be coherent, and their acquisitions reveal the same scene. Consequently, the dual-band acquisition is suitable for an enhanced radar imaging processing. The development of the processing algorithms exploiting the coherent dual-band operation is in progress, and is out of the scope of this article, which focuses on the demonstration of the coherent dual-band photonics-based radar hardware developed on a photonic chip.

V. CONCLUSION

The first photonics-based dual-band radar system with the transceiver developed on a photonic chip has been presented, characterized, and tested in an outdoor field trial in a relevant maritime scenario. The photonics-based radar transceiver has been designed and implemented on a SOI technology platform for frequency-agile operation up to the Ku-band. The bare PIC characterization has confirmed the designed innovative frequency agility for both the transmitter and the receiver with very good performance in terms of linearity, SFDR, and sensitivity. The main issue is given by the conversion loss > 50 dB that largely exceeds the value of standard RF systems (for RF mixers, the conversion loss can be <20 dB). This high value is basically due to the optical losses in the PIC, and to the low efficiency in the electro-optical conversion. Technological advancements for reducing the optical loss of the PICs is expected to come from introducing optical amplification stages, as is currently largely studied for example by means of hybrid integration of active PICs (e.g., in Indium Phosphide) on Silicon [26]–[29]. A further improvement can be obtained improving the electro-optical conversion efficiency, with possible solutions form developing modulators with higher linearity and lower Vpi voltage [30].

After the characterization, the bare PIC has been packaged and engineered on a PCB. The symmetric structure of the transmitter and receiver included in the PIC has been exploited for simplifying the packaging and the design of the control PCB with a modular approach, using two replicas of the PIC to implement the transmitter and the receiver units, respectively, using two identical PCBs. The characterization of the engineered PIC reveals few dB of penalty on the conversion loss and SFDR introduced by the packaging operations. The phase noise of the systems has been also measured, confirming the expected performance.

The development of two front-ends operating in S- and X-band respectively, has allowed to test the complete radar system in a dual-band configuration. Despite the high conversion loss of the PIC, the sensitivity measurement and the tow-tone analysis on the complete system confirm performance aligned with the RF state of the art for what concerns the dynamic range and the sensitivity, while maintaining the innovative feature of the coherent dual-band operation.

Finally, the proposed photonics-based dual-band radar system has been moved in a site close to the port of Livorno (Italy) for an outdoor field trial in relevant maritime scenario. The detection results from the field trial, also compared with AIS official data, confirm not only the effectiveness of the radar system in detecting range and Doppler of targets, but also good performance in terms of false alarm probability (2×10^{-5}). The range resolution has been defined by the front-end bandwidth to 7.5 m, while the cross-range resolution has been given by the antenna apertures. The dual band operation has been also verified, detecting the same scene exploiting coherent radar signals in S- and X- band and obtaining congruous results.

It is worth underlining that the radar field trial has not aimed at demonstrating innovative performance. Rather, the innovation here is given by (i) the developed hardware enabling – for the first time to our knowledge – a coherent dual-band radar operation exploiting integrated photonics, and by (ii) its validation in a real field trial, demonstrating the innovative frequency agility feature while preserving state of the art performance.
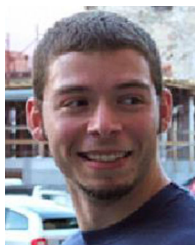
This work now opens the way to the development of processing algorithms to exploit the coherent dual-band acquisitions for enhanced target imaging and scene reconstruction [31]. Moreover, the demonstrated use of photonic integration allows reducing the SWaP of radar systems and, although technological developments are still needed, opens the way to smarter surveillance systems based on mobile and compact platforms [32].
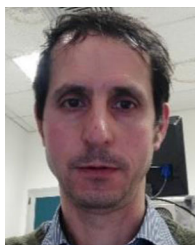
REFERENCES

[1] M. A. Richards *et al.*, *Principles of Modern Radar*. Raleigh, NC USA: SciTech Pub, 2010.

[2] M. I. Skolnik, *Radar Handbook*. New York, NY, USA: McGraw-Hill Education, 2008.

[3] H. Myers, R. Moore, W. Butler, and S. Ware, "Common aperture multiband radar (CAMBR)," in *Proc. Nat. Radar Conf.*, May 1997, pp. 143–148.

[4] J. Tian, J. Sun, G. Wang, Y. Wang, and W. Tan, "Multiband radar signal coherent fusion processing with IAA and apFFT," *IEEE Signal Process. Lett.*, vol. 20, no. 5, pp. 463–466, May 2013.

[5] P. van Dorp, R. Ebeling, and A. G. Huizing, "High resolution radar imaging using coherent multiband processing techniques," in *Proc. 2010 IEEE Radar Conf.*, 2010, pp. 981–986.

[6] F. Rodriguez-Moreles *et al.*, "A compact, reconfigurable, multi-UWB radar for snow thickness evaluation and altimetry: Development and field trials," *IEEE J. Sel. Topics Appl. Earth Observ. Remote Sens.*, vol. 14, pp. 6755–6765, 2021.

[7] F. Fioranelli *et al.*, "Practical investigation of multiband mono- and bistatic radar signatures of wind turbines," *IET Radar, Sonar Navig.*, vol. 11, no. 6, pp. 909—921, 2017.

[8] J. Capmany and D. Novak, "Microwave photonics combines two worlds," *Nature Photon.*, vol. 1, pp. 319–330, 2007.

[9] J. Yao, "Microwave photonics," *J. Lightw. Technol.*, vol. 27, no. 3, pp. 314–335, 2009.

[10] P. Ghelfi *et al.*, "A fully photonics-based coherent radar system," *Nature*, vol. 507, pp. 341–345, 2014.

[11] S. Pan and Y. Zhang, "Microwave photonic radars," *J. Lightw. Technol.*, vol. 38, no. 19, pp. 5450–5484, 2020.

[12] E. A. Kittlaus *et al.*, "A low-noise photonic heterodyne synthesizer and its application to millimeter-wave radar," *Nature Commun.*, vol. 12, 2021, Art. no. 4397.

[13] F. Zhang *et al.*, "Photonics-based real-time ultra-high-range-resolution radar with broadband signal generation and processing," *Sci. Reports*, vol. 7, 2017, Art. no. 13848.

[14] F. Laghezza *et al.*, "Field evaluation of a photonics-based radar system in a maritime environment compared to a reference commercial sensor," *IET Radar, Sonar Navig.*, vol. 9, no. 8, pp.1040–1046, 2015.

[15] S. Maresca, P. Ghelfi, G. Serafino, A. Bogoni, and F. Scotti, "Field trial of a coherent widely distributed dual-band photonics-based radar network in a real maritime environment," in *Proc. Int. Topical Meeting Microw. Photon.*, Nov. 2021, pp. 1–4.

[16] P. Ghelfi *et al.*, "Photonics for radars operating on multiple coherent bands," *J. Lightw. Technol.*, vol. 34, no. 2, pp. 500–507, 2016.

[17] X. Zhang *et al.*, "Novel RF-source-free reconfigurable microwave photonic radar," *Opt. Exp.*, vol. 28, no. 9, pp. 13650–13661, 2020.

[18] A. Wang *et al.*, "Microwave photonic radar system with ultra-flexible frequency-domain tunability," *Opt. Exp.*, vol. 29, no. 9, pp. 13887–13898, 2021.

[19] G. Serafino *et al.*, "A photonics-assisted multi-band MIMO radar network for the port of the future," *IEEE J. Sel. Topics Quantum Electron.*, vol. 27, no. 6, pp. 1–13, Nov./Dec. 2021, Art. no. 6000413.

[20] M. Chen *et al.*, "A silicon integrated microwave-photonic transceiver," in *Proc. Opt. Fiber Commun. Conf. Exhib.*, 2017, pp. 1–3.

[21] S. Li *et al.*, "Chip-Based microwave-photonic radar for high-resolution imaging," *Laser Photon. Rev.*, vol. 14, no. 10, 2020, Art. no. 1900239.

[22] F. Falconi *et al.*, "A combined radar & lidar system based on integrated photonics in Silicon-on-Insulator," *IEEE J. Lightw. Technol.*, vol. 39, no. 1, pp. 17–23, Jan. 2021.

[23] S. Melo *et al.*, "A silicon integrated photonics-based radar operating in multiple bandwidths," in *Proc. Int. Topical Meeting Microw. Photon.*, 2020, pp. 47–49.

[24] F. Scotti *et al.*, "Indoor field-trial in X band of a photonics-based multiband radar on a packaged silicon chip," in *Proc. Int. Topical Meeting Microw. Photon.*, 2021, pp. 1–4.

[25] W. Bogaerts *et al.*, "Nanophotonic waveguides in silicon-on-insulator fabricated with CMOS technology," *J. Lightw. Technol.*, vol. 23, no. 1, pp. 401–412, 2005.

[26] G.-H. Duan *et al.*, "Hybrid III–V on silicon lasers for photonic integrated circuits on silicon," *IEEE J. Sel. Topics Quantum Electron.*, vol. 20, no. 4, pp. 158–170, Jul./Aug. 2014, Art. no. 6100213.

[27] T. Matsumoto *et al.*, "Hybrid-integration of SOA on silicon photonics platform based on flip-chip bonding," *IEEE J. Lightw. Technol.*, vol. 37, no. 2, pp. 307–313, Jan. 2019.

[28] Y. Fan *et al.*, "Hybrid integrated InP-Si$_3$N$_4$ diode laser with a 40-Hz intrinsic linewidth," *Opt. Exp.*, vol. 28, no. 15, pp. 21713–21728, 2020.

[29] C. O. De Beeck *et al.*, "Heterogeneous III–V on silicon nitride amplifiers and lasers via microtransfer printing," *Optica*, vol. 7, no. 5, pp. 386–393, 2020.

[30] M. He, "High-performance hybrid silicon and lithium niobate mach–zehnder modulators for $100 \, \mathrm{Gbit \, s^{-1}}$ and beyond," *Nature Photon.*, vol. 13, pp. 359–364, 2019.

[31] D. Xiong *et al.*, "BSBL-based multiband fusion ISAR imaging," *IET J. Eng.*, vol. 2019, no. 19, pp. 6039–6042, 2019.

[32] M. Mandlik, C. Sturm, U. Lübbert, T. Vajdiak, and J. Kubak, "Multiband automotive radar sensor with agile bandwidth," in *Proc. IEEE-APS Topical Conf. Antennas Propag. Wireless Commun.*, 2017, pp. 163–165.
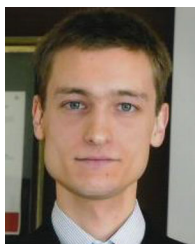
Giovanni Serafino received the Ph.D. degree (*cum laude*) in emerging digital technologies from the Sant'Anna School of Advanced Studies, Pisa, Italy, in 2013. He is currently an Assistant Professor with the Sant'Anna School of Advanced Studies. His research interests include optical signal processing, fiber-optic transmission systems, reconfigurable nodes for optical networks, applications of microwave photonics techniques to radar systems, and wireless communications, including optical beamforming for 5G and photonics-assisted coherent MIMO radars. He is a coauthor of more than 20 papers on international journals and more than 60 papers on conference proceedings, two book chapters, and five patents.

Antonio Malacarne received the M.S. degree (with Hons.) in telecommunication engineering from the University of Pisa, Pisa, Italy, in 2004, and the Ph.D. degree (with Hons.) in emerging digital technologies from the Sant'Anna School of Advanced Studies, Pisa, Italy, in 2009. He was an Assistant Professor with the Sant'Anna School of Advanced Studies till 2020. He is currently a Senior Researcher with the CNIT – National Inter-University Consortium for Telecommunications, Photonic Networks and Technologies National Laboratory, Pisa, Italy, within the microwave photonics for communication and sensing area. He is a coauthor of 49 papers on international scientific journals, more than 100 papers on international conference proceedings, 11 international patents, and three book chapters. His teaching activity mainly include coherent optical systems, optical interconnects, photonics for switching, and remote sensing. His scientific interests include optical signal processing of ultra-fast signals and optical transmission, and microwave photonics for remote sensing and biophotonics.

Salvatore Maresca received the M.S. degree in telecommunications engineering and the Ph.D. degree in information engineering from the University of Pisa, Pisa, Italy, in 2006 and 2010, respectively. In July 2010, he joined the NATO Centre for Maritime Research and Experimentation, La Spezia, Italy. In 2016, he joined the CNIT, Pisa. Since January 2018, he has been a Senior Researcher with the TeCIP Institute, Sant'Anna School of Advanced Studies, Pisa, Italy. He is currently with CNR. He has authored or coauthored more than 35 scientific and technical publications and reports, and two book chapters. His research interests include statistical signal processing of radar data, with a special focus on sea clutter analysis, target detection and tracking strategies, data, and information fusion in MIMO radars.

Malik Muhammad Haris Amir received the undergraduation degree in electrical engineering from Air University, Islamabad, Pakistan, in 2014, the master's degree in electrical engineering from the National University of Science and Technology and the second master's degree in photonic integrated circuits, sensors, and networks within the PIXNET program of Erasmus Mundus from Sant'Anna School, Pisa, Italy, where he has been working toward the Ph.D. degree since 2020. The main area of his Ph.D. research is Coherent MIMO Radars Processing.

Claudio Porzi received the M.S. degree in electronics engineering from the University of Rome, La Sapienza, Italy, in 2000, and the Ph.D. degree in telecommunications from Scuola Superiore Sant'Anna, Pisa, Italy, in 2005. He is currently an Assistant Professor with the Institute of Communication, Information, and Perception Technologies, Scuola Superiore Sant'Anna, within the digital and microwave photonics research area, working on the design and characterization of photonic integrated circuits for telecom and microwave photonics applications. He has coauthored more than 150 research articles published in peer-reviewed journals or presented at international conferences, in the fields of optical communications, microwave photonics, and photonic integrated circuits, and holds six international patents. He was the recipient of the Best Paper Award at the International Communications Conference in 2010 and of the Charles Kao Award for Best Optical Communications and Networking Paper in 2017.

Paolo Ghelfi received the M.Sc. degree in electronic engineering in 2000. Since 2001, he has been with PNT Laboratory, CNIT, Pisa, Italy, where he is currently the Head of Research Area. He has authored or coauthored more than 40 papers on international journals, more than 110 papers on international conferences, more than 20 patents, and two book chapters. His current research interests include microwave photonics, with strong experience also in the fields of high bit rate fiber-optic transmission systems, all-optical signal processing, and reconfigurable networks.

Antonella Bogoni is currently a Full Professor with the Sant'Anna School of Advanced Studies, Pisa, Italy, and the Director of the PNT Laboratory, CNIT, Pisa, Italy. Her research interests include photonics technologies for optical fiber networks for ultrafast optical signal processing and microwave systems, especially for 5G, radars, and space applications. Moreover, she is leading the design of specific photonic integrated circuits for implementing on-chip the proposed solutions. She has been scientific responsible for 48 grants (27 as PI or coordinator). She has authored or coauthored 56 patents, eight books and chapters, and more than 160 papers on the main scientific international journals (22 invited contributions). She has more than 300 contributions in the main photonics and radar international conferences, winning nine best paper awards, with more than 90 invited contributions. In 2014 and 2020, she was the Topical Editor of *Optics Letters* and guest editors of nine special issues on international journals. She is the Chair of conferences and workshops, including the General Chair of MWP 2021 and Photonics in Switching 2014, Program Chair of ECOC 2018.

Filippo Scotti received the M.Sc. degree in physics engineering from the Politecnico di Milano, Milan, Italy, in 2009. In 2009, he was with the PGT-Photonics, Milan, Italy, for a six-month internship. Since 2010, he has been a Researcher with CNIT, Pisa, Italy. He has authored or coauthored more than 60 papers in international journals and conferences, holding five patents. His research interests include microwave photonics for radar and sensing applications and fiber optic transmissions with particular inter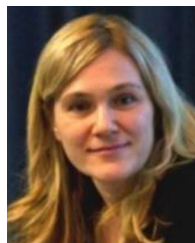est in all-optical signal processing.